ROYAL SOCIETY
OF CHEMISTRY

PAPER

Check for updates

An up-conversion luminophore with high quantum yield and brightness based on BaF₂:Yb³⁺,Er³⁺ single crystals†

Eduard I. Madirov,[ab] Vasilii A. Konyushkin,[c] Andrey N. Nakladov,[c] Pavel P. Fedorov,[c] Thomas Bergfeldt, [d] Dmitry Busko,[b] Ian A. Howard, [be] Bryce S. Richards, [be] Sergey V. Kuznetsov*[c] and Andrey Turshatov *[b]

Up-conversion (UC) of near-infrared radiation to visible light has received much attention because of its use in the conversion of solar radiation, luminescence thermometry, biosensing, and anti-counterfeiting applications. However, the main issue hindering the successful utilization of UC is the relatively low quantum efficiency of the process. In order to design new UC systems with high quantum yield (ϕ_{UC}) values, we synthesized two series of co-doped BaF₂ single crystals with nominal concentrations of Yb³⁺ (2–15 mol%)/Er³⁺ (2 mol%) as well as Yb³⁺ (3 mol%)/Er³⁺ (2–15 mol%). The highest ϕ_{UC} value of 10.0% was demonstrated for the BaF₂:Er³⁺ (2 mol%) and Yb³⁺ (3 mol%) sample under 490 W cm⁻² of 976 nm excitation. To study the natural limit of UC efficiency, quantum yield values upon direct excitation (ϕ_{DS}) of the ⁴S₃/₂ ($\phi_{DS} \leq 4\%$) and ⁴F₉/₂ ($\phi_{DS} \leq 26\%$) levels were measured. Comparison of experimental values of quantum yields to the ones obtained using Judd–Ofelt theory reveals strong quenching of the ⁴S₃/₂ state for all investigated compositions. In addition, we observed an unusually strong contribution of the Er³⁺:⁴I₉/₂ excited state to both UC and down-shifting luminescent processes. This contribution becomes possible due to the very low maximum phonon energy of BaF₂ crystals (240 cm⁻¹).

Introduction

Luminescent materials based on lanthanide ions – ranging from molecular complexes to inorganic phosphors – remain not only interesting from a scientific point of view but also relevant for many new applications.[1,2] These applications include optical nanoprobes for medical usage,[3–7] colour conversion materials for light emitting diodes,[8,9] organic light emitting diodes,[10] solar radiation converters,[11–13] luminescent thermometers[14–17] and inks used for anti-counterfeiting purposes.[18,19] In general, the luminescence of lanthanide-based materials can be divided into two main types: Stokes

and anti-Stokes. The majority of known luminescence materials exhibit Stokes emission, also known as down-shifted (DS) emission, meaning that emitted photons have lower energy than absorbed ones. Fewer materials exhibit anti-Stokes emission, where emitted photons have higher energy than the absorbed ones.

Anti-Stokes emission, the so called the up-conversion (UC) process, based on trivalent lanthanide ions (Ln³⁺) can reach high photoluminescence quantum yields of 5–11% under relatively low excitation intensity (<40 W cm⁻²),[20–23] in contrast to high light intensity (>10⁶ W cm⁻²) required for other prominent anti-Stokes processes such as multi-photon absorption and multi-harmonic generation.[24] Thus, lower-power light emitting diodes[25] or even xenon lamp (for a special case of dye-synthesized UC)[26] can be used as excitation sources in lanthanide based UC. Four main UC mechanisms generally considered are ground state absorption with a subsequent excited state absorption (GSA/ESA), energy transfer UC (ETU), cooperative UC and photon avalanche UC.[27,28] The ETU is the most efficient mechanism among these four and occurs at high Ln³⁺ concentrations (>2 mol%) and moderate excitation intensity.[29,30] At lower doping concentrations or higher excitation intensities, GSA/ESA can occur simultaneously with the ETU process or even start playing a dominant role.[31]

ᵃ Kazan Federal University, Kremlyovskaya str, 18, Kazan, 420008, Russia

ᵇ Institute of Microstructure Technology, Karlsruhe Institute of Technology (KIT), Hermann-von-Helmholtz-Platz 1, Eggenstein-Leopoldshafen, 76344, Germany. E-mail: andrey.turshatov@kit.edu

ᶜ Prokhorov General Physics Institute of the Russian Academy of Sciences (GPI RAS), Vavilov str, 38, Moscow, 119991, Russia. E-mail: kouznetzovsv@gmail.com

ᵈ Institute for Applied Materials, Karlsruhe Institute of Technology (KIT), Hermann-von-Helmholtz-Platz 1, Eggenstein-Leopoldshafen, 76344, Germany

ᵉ Light Technology Institute, Karlsruhe Institute of Technology (KIT), Engesserstrasse 13, Karlsruhe, 76131, Germany

† Electronic supplementary information (ESI) available. See DOI: 10.1039/d1tc00104c

This journal is © The Royal Society of Chemistry 2021

J. Mater. Chem. C, 2021, **9**, 3493–3503 | **3493**

In order to increase the efficiency of the UC, co-doping with a material (called sensitizer) that has a high absorption cross-section can be utilized. If the goal is to achieve UC from the near-infrared (NIR) to visible (Vis) region, then co-doping with Yb^{3+} ions is often applied. The $^2F_{7/2} \rightarrow {}^2F_{5/2}$ transition of the Yb^{3+} is resonant with the f–f transitions of Er^{3+}, Tm^{3+}, and Ho^{3+} ions, thus providing efficient energy transfer. Thereby, Er^{3+}/Yb^{3+}, Ho^{3+}/Yb^{3+}, and Tm^{3+}/Yb^{3+} pairs are often used in the NIR-to-Vis UC systems.[32–37]

Another important factor for the efficient UC process is the host matrix, as it affects the environment around the optical centres. The host matrix has to have low phonon energy in order to minimize the non-radiative losses and favour radiative transitions. In a wide range of UC materials, fluorides are optimal candidates for use as the host due to their relatively low phonon energies and good chemical stability.[38,39] Recently, we investigated SrF_2:Yb^{3+},Er^{3+} single crystals and reported a very high UC quantum yield of 6.5%.[23] Inspired by this work, we assumed that a BaF_2 single crystal with maximum phonon energy of 240 cm^{-1}, which is significantly lower than the phonon energy of other prominent fluoride hosts (β-$NaYF_4$ – 360 cm^{-1},[40] LaF_3 – 350 cm^{-1},[41] CaF_2 – 320 cm^{-1}[42] and SrF_2 – 284 cm^{-1}[42]), is a good candidate for further improving the UC efficiency.

It is known that the normally forbidden f–f transitions in rare-earth element (Ln^{3+}) ions become partially allowed in materials with a low crystal symmetry and strong local distortion of the crystal field. Though, the BaF_2 crystal (as well as SrF_2 and CaF_2 hosts) exhibits a high cubic crystal symmetry with a fluorite structure which is usually not favourable for an efficient UC process.[43] However, co-doping with Yb^{3+} and Er^{3+} occurs via the substitution of the divalent cation and requires charge compensation via negative fluorine ions (F^-) in interstitial positions. These interstitial anions reduce the symmetry of Ln^{3+} single ion centres giving rise to trigonal and tetragonal symmetry and, thus, increase the probability of radiative transitions.[44] Moreover, at higher dopant concentrations preferential clustering of lanthanide ions occurs, which can reduce inter-ionic distances and enhance both ETU and cross-relaxation processes.[45,46]

There have been a number of studies dedicated to the optical properties of BaF_2 doped with Er^{3+} and Yb^{3+} ions. The majority of works have used glasses or glass ceramics.[47–50] Although these studies provide some insight into their UC behaviour, a more extensive study of the optical properties is required in order to get a more detailed picture of UC properties of BaF_2-based materials. Thus, the focus of this work is (i) to assess how efficient UC in the BaF_2 host can be via measurements of the absolute quantum yield in an integrating sphere (ϕ_{UC}) for different concentrations of doping ions and (ii) to provide a more detailed understanding of UC mechanism in the BaF_2 host (via the study of both UC and DS luminescent properties). In this context, single-crystals of BaF_2 are great study objects because of two reasons (i) lack of grain boundaries reduces light scattering and ensures efficient dissipation of heat produced within non-radiative relaxation of excited ions[51–55] and (ii) large volume to surface ratio allows neglecting the surface quenching effect and improves chemical stability of the samples.

Experimental

Synthesis and characterization

Barium fluoride, ytterbium fluoride and erbium fluoride were highly pure (99.99% LANHIT, Russia). The powders of the fluoride precursors were preliminarily melted under a CF_4 fluorinating atmosphere. Afterwards, the fluoride single crystals were grown by the Bridgman technique in a vacuum furnace under a CF_4 fluorinating atmosphere. Both the heater with a temperature gradient (60–80 K cm^{-1}) and the crucible were made up of graphite. The temperature (1360 °C) and crystallization velocity (6.5 mm per hour) were chosen based on the phase diagrams of BaF_2–Ln^{3+}.[56,57] The grown crystals are 5 cm long rods with 10 mm diameter. The crystals were cut in the direction perpendicular to the long axis and resulting discs (thickness of 2 mm and diameter of 10 mm) were polished for optical measurements.

Two series of the single-crystal BaF_2 crystals doped with Er^{3+} and Yb^{3+} ions were grown by the Bridgman technique. The first series consisted of BaF_2 doped with nominal concentrations of 2 mol% of Er^{3+} ions and 2, 3, 5, 7, 10, 15 mol% of Yb^{3+} (hereafter the mol% represents the nominal concentration of the Ln^{3+} ions used in the synthesis of the crystals, whereas the exact compositions estimated via wavelength-dispersive X-ray fluorescence (WDXRF) spectroscopy are reported in Table S1, ESI†). The second series is doped with 3 mol% of Yb^{3+} ions as well as 3, 5, 10, 15 mol% of Er^{3+} ions. These concentration ranges were chosen because the previous research has revealed a strong concentration quenching and deteriorated UC luminescence at higher doping concentrations of both ions.[58]

The crystalline structure of the samples was determined using the powder XRD patterns recorded with a Bruker D2 PHASER diffractometer (CuKα radiation). For this purpose, a small part of the single crystal was ground into powder. The patterns were recorded in the 2 theta range from 10 to 70 degrees.

The concentration of elements Ba^{2+}, Er^{3+} and Yb^{3+} were determined by WDXRF spectroscopy (Pioneer S4, from Bruker AXS). For the measurement, three replicates of each sample were analyzed. 25 mg of the sample material (accuracy ± 0.05 mg) were dissolved with 6 g EQF-TML-5050-5 (49.75% $Li_2B_4O_7$ + 49.75% $LiBO_2$ + 0.5% LiBr) in a platinum crucible at 1373 K. After cooling in a platinum stencil the fusion tablet was analyzed. For the calibration, four fusion tablets with matrix-adapted standards (BaF_2, Er_2O_3, and Yb_2O_3) were melted. Two to three energy lines of the elements were used for the calculation. The standard deviation in the determination of the chemical composition did not exceed 0.6 wt% for barium, 0.07 wt% for erbium, and 0.05 wt% for ytterbium.

Optical methods

The Raman spectrum for the undoped BaF_2 sample was recorded with an i-Raman device by Polytec (785 nm excitation, 3.5 cm^{-1} resolution).

The refractive indices of the samples were measured with a Metricon 2010/M prism coupler using 1550 nm laser radiation

3494 | J. Mater. Chem. C, 2021, 9, 3493–3503

This journal is © The Royal Society of Chemistry 2021

(Thorlabs, TLK-L1550R). The detailed description of the setup was reported earlier.[59]

Absorption spectra were recorded at room temperature using a UV-Vis spectrometer PerkinElmer Lambda 950 in the absorbance mode. The absorption coefficient was calculated using the following expression in eqn (1):

$$\alpha = -\frac{1}{d}\ln\left(10^A\right) \qquad (1)$$

where α is the absorption coefficient in cm^{-1}, A is the absorbance data obtained from the device, and d is sample thickness in centimetres. The excitation spectra were recorded using a calibrated spectrophotometer Varian Cary Eclipse.

The setup and the methodology for the estimation of ϕ_{UC} under 976 nm excitation have been described previously.[23,60] To record ϕ_{DS} of the $^4S_{3/2} \rightarrow {}^4I_{15/2}$ and $^4F_{9/2} \rightarrow {}^4I_{15/2}$ transitions of the Er^{3+} ions a tunable CW laser (SolsTis with EMM-Vis, M-Squared Lasers Ltd) pumped by a 532 nm laser (Verdi-V18, Coherent) was utilized. The system was tuned to 522 nm for the direct excitation of the $^4S_{3/2}$ level and to 652 nm for the direct excitation of the $^4F_{9/2}$ level. For the measurement of ϕ_{DS} of the $^4I_{13/2} \rightarrow {}^4I_{15/2}$ transition upon direct excitation, a tunable laser kit (Thorlabs, TLK-L1550M) operating at 1520 nm was used as the excitation source. The remaining setup was the same as described in our earlier publication.[60]

Luminescence lifetimes of the emissive levels were measured with a home-built optical system described previously.[61] Briefly, 525 nm, 976 nm, and 633 nm (Roithner) and 1550 nm (Thorlabs) laser diodes mounted in temperature stabilized mounts (TCLDM9, Thorlabs) and driven by a laser diode controller (ITC4001, Thorlabs) as well as 375 nm LED also driven by the controller (ITC4001, Thorlabs) were used as the excitation sources. The power of the laser beam was adjusted with a controlled rotatable neutral density filter (Thorlabs). The remaining setup was the same as described in our previous publication.[59]

Results and discussion

Crystal structure characterization

The measured powder XRD patterns are presented in Fig. 1 together with JCPDS card 04-0452 (BaF$_2$). The unit cell parameters (a) calculated from the XRD data are given in Table S1 (ESI†). They are in a good agreement with the values of the BaF$_2$ unit cell parameter (a = 6.200 Å) available in the literature.[62] It is observed that the unit cell parameter decreases with the increase of doping concentration of both Yb^{3+} and Er^{3+}. This may be attributed to the fact that ionic radii of Er^{3+} and Yb^{3+} ions are smaller than that of Ba^{2+}.[63] This discrepancy results in a lower volume of the unit cell and reduced distance between doping ions, which, in turn, allows for a higher local concentration of the doping ions.

Raman spectroscopy was performed for the undoped BaF$_2$ crystalline sample. The spectrum has one distinct peak at 240 cm^{-1} (Fig. S1, ESI†), which perfectly correlates to the value of ~240 cm^{-1} observed earlier in several other publications,[42,64] and reveals low phonon energy of the BaF$_2$ host.
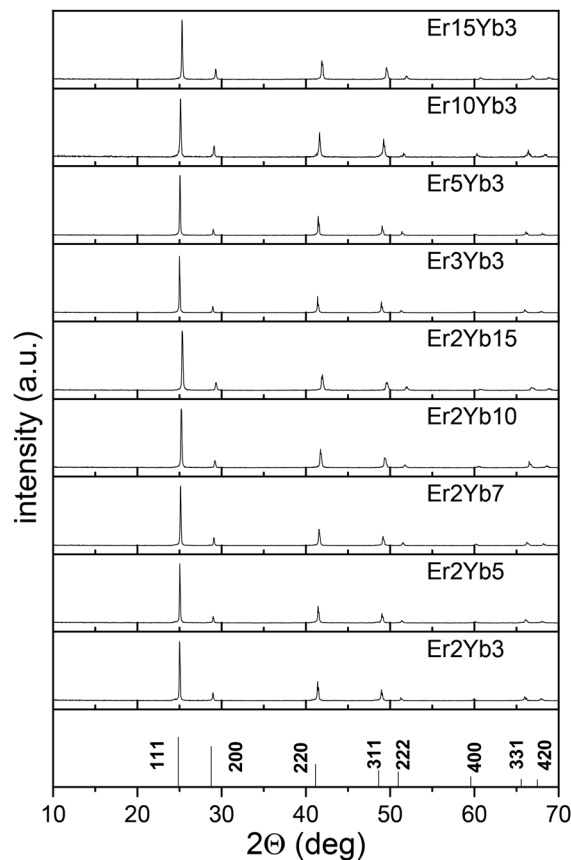

Fig. 1 Powder XRD patterns of the BaF$_2$:Yb^{3+}, Er^{3+} samples.

In addition, the exact chemical composition of the samples was studied by WDXRF spectroscopy. The obtained weight% of the doping ions, *via* the WDXRF method, allowed the calculation of the mol% values that represent the fraction of the Ba cations substituted with rare-earth ions. The resulting values are given in Table S1 (ESI†). For the sake of clarity, we will use the nominal concentrations of Er^{3+} and Yb^{3+} (related to the sample names) in further discussion. The uncertainties for the concentrations were 0.30 wt%, 0.02 wt%, and 0.02 wt% for barium, erbium, and ytterbium, respectively.

Optical characterization

Absorption and luminescence spectra

The absorption spectra shown in Fig. 2 demonstrate absorption bands in ultraviolet (UV), Vis and near infrared (NIR) ranges, characteristic of Er^{3+} and Yb^{3+} ions. The narrow absorption bands arise from the f–f transitions of the Er^{3+} and Yb^{3+} ions. The positions of the lines are in accordance with the literature data.[23,32,33] The shape of the peaks remains the same in all samples. It demonstrates that the local environment of the doping ions is consistent and there are no strong local deformations of the crystal structure in the investigated range of doping concentrations.

Table 1 displays the values of the peak absorption cross-sections of the most prominent absorption bands of Er^{3+} and
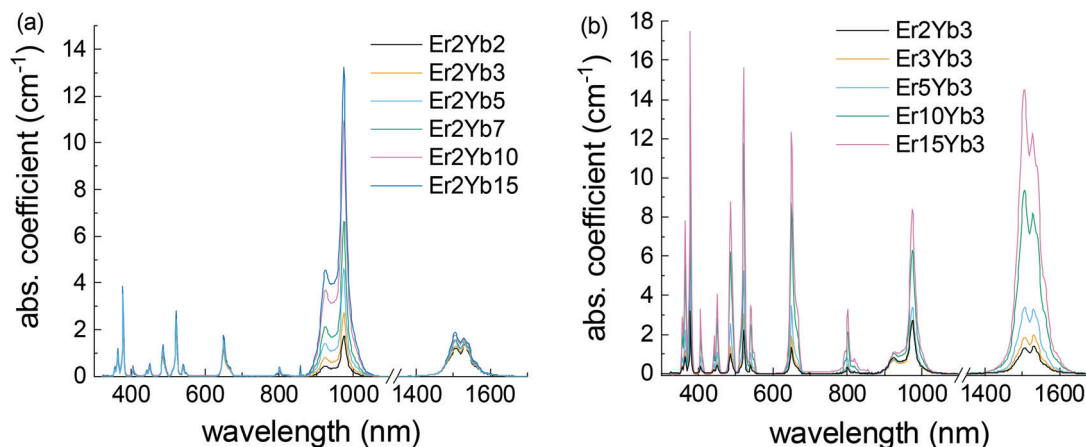
This journal is © The Royal Society of Chemistry 2021

J. Mater. Chem. C, 2021, **9**, 3493–3503 | **3495**

Fig. 2 Absorption spectra of two series of co-doped BaF_2 single crystals (a) samples with fixed Er^{3+} concentration whereas Yb^{3+} concentration varied from 2 to 15 mol% and (b) samples with fixed Yb^{3+} concentration where Er^{3+} concentration varies from 2 to 15 mol%.

Table 1 Peak absorption cross-sections for optical transitions in Er^{3+} and Yb^{3+} ions, pm^2

	378 nm $Er^{3+}:^4I_{15/2} \rightarrow {}^4G_{11/2}$	406 nm $Er^{3+}:^4I_{15/2} \rightarrow {}^2H_{9/2}$	450 nm $Er^{3+}:^4I_{15/2} \rightarrow {}^4F_{5/2}$	522 nm $Er^{3+}:^4I_{15/2} \rightarrow {}^2H_{11/2}$	650 nm $Er^{3+}:^4I_{15/2} \rightarrow {}^4F_{9/2}$	1506 nm $Er^{3+}:^4I_{15/2} \rightarrow {}^4I_{13/2}$	976^a nm $Yb^{3+}:^2F_{7/2} \rightarrow {}^2F_{5/2}$
Er2Yb2	0.91	0.09	0.12	0.64	0.40	0.37	0.52
Er2Yb3	0.98	0.11	0.13	0.68	0.42	0.40	0.62
Er2Yb5	1.25	0.13	0.16	0.87	0.54	0.52	0.69
Er2Yb7	1.23	0.14	0.18	0.89	0.55	0.56	0.70
Er2Yb10	1.31	0.16	0.20	0.97	0.61	0.62	0.69
Er2Yb15	1.28	0.15	0.19	0.94	0.58	0.62	0.66
Er3Yb3	1.01	0.11	0.14	0.73	0.46	0.44	
Er5Yb3	0.99	0.13	0.16	0.76	0.51	0.49	
Er10Yb3	0.99	0.16	0.21	0.86	0.64	0.68	
Er15Yb3	0.81	0.15	0.19	0.73	0.57	0.67	

^{a} The absorption cross-section of the $Yb^{3+}:^2F_{7/2} \rightarrow {}^2F_{5/2}$ transition was calculated only for the samples with 2% of Er^{3+}, because at higher doping concentrations the contribution of the Er^{3+} absorption results in the overestimation of the absorption cross-section.

Yb^{3+}. For instance, the peak cross-section of the $Yb^{3+}:^2F_{7/2} \rightarrow {}^2F_{5/2}$ absorption band is 0.62–0.7 pm^2 in the concentration range of Yb^{3+} of 3–15 mol%. The absorption cross-section of the $Yb^{3+}:^2F_{7/2} \rightarrow {}^2F_{5/2}$ transition was calculated only for the samples with 2% of Er^{3+} because at higher doping concentrations the contribution of the Er^{3+} absorption becomes significant at this wavelength.

The values are in line with the absorption cross-section values of the Er^{3+} and Yb^{3+} ions in hosts with a comparable structure available in the literature.[23,45,65–67] Overall, Yb^{3+} ions in the BaF_2 host demonstrate absorption cross-section comparable to values reported for CaF_2 (0.55 pm^2)[66] and SrF_2 (0.89 pm2),[67] whereas absorption cross-section in oxide crystals is usually higher. For example, Yb^{3+} absorption cross-sections of 0.8 pm^2 in YAG,[68] 1.7 pm^2 in Gd_2O_3,[69] and 8 pm^2 in $GdVO_4$[70] were previously reported. Another noticeable trend in the data is the significant increase in the absorption cross-section of Er^{3+} bands with the increase of both Er^{3+} and Yb^{3+} doping concentrations.
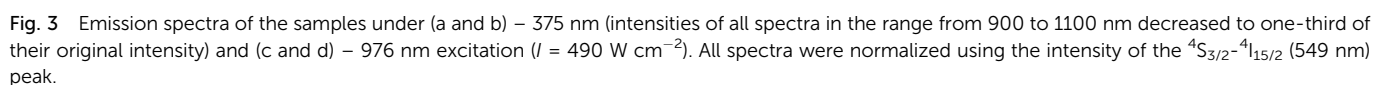
This phenomenon has already been reported by Auzel et al.[71] and may be attributed to the fact that trivalent Er^{3+} and Yb^{3+} ions substitute divalent Ba^{2+} ions in the crystal. Higher amounts of the doping ions create stronger local distortion of

the crystal field that favours the radiative transitions in the Ln^{3+} ions.[45]

The emission spectra of co-doped BaF_2 crystals are presented in Fig. 3. The DS emission spectra obtained under 375 nm excitation ($^4G_{11/2}$ level of the Er^{3+} ions) are given in Fig. 3a and b while the UC emission spectra obtained under 976 nm excitation ($^2F_{5/2}$ level of the Yb^{3+} ion) are shown in Fig. 3c and d. All spectra have typical emission bands of the Er^{3+} and Yb^{3+} ions with the emission of Er^{3+} ions located around 405 nm ($^2H_{9/2} \rightarrow {}^4I_{15/2}$), 521 nm ($^2H_{11/2} \rightarrow {}^4I_{15/2}$), 540 nm ($^4S_{3/2} \rightarrow {}^4I_{15/2}$), 650 nm ($^4F_{9/2} \rightarrow {}^4I_{15/2}$), 810 nm ($^4I_{9/2} \rightarrow {}^4I_{15/2}$) and 850 nm ($^4S_{3/2} \rightarrow {}^4I_{13/2}$) and the emission of {$Er^{3+}:^4I_{11/2}$ & $Yb^{3+}:^2F_{5/2}$} manifold at 1020 nm. The position of these transitions on the energy level diagram is additionally given in Fig. S2 (ESI†). Under 375 nm excitation, the relative intensities of the Er^{3+} emission bands do not exhibit a strong dependence on the doping concentrations of Yb^{3+} until it reaches 10 mol% (see Fig. 3a). At this point, the relative intensity at 668 nm strongly increases, indicating two possible effects: (i) a strong depopulation of the $^4S_{3/2}$ level and/or (ii) an extra population of the $^4F_{9/2}$ level. The $^2H_{9/2} \rightarrow {}^4F_{9/2}$ transition in Er^{3+} is resonant with the $^2F_{7/2} \rightarrow {}^2F_{5/2}$ transition in Yb^{3+}[72] (as shown in Fig. S2, ESI,† transition ①). If existing, these

3496 | J. Mater. Chem. C, 2021, 9, 3493–3503

This journal is © The Royal Society of Chemistry 2021

Fig. 3 Emission spectra of the samples under (a and b) − 375 nm (intensities of all spectra in the range from 900 to 1100 nm decreased to one-third of their original intensity) and (c and d) − 976 nm excitation (I = 490 W cm^{-2}). All spectra were normalized using the intensity of the $^4S_{3/2}$-$^4I_{15/2}$ (549 nm) peak.

transitions lead to both a lower population of the $^4S_{3/2}$ level and an increase of the $^4F_{9/2}$ level population in line with the results presented in the Fig. 3a. The increase in the {Er^{3+}:$^4I_{11/2}$ & Yb^{3+}:$^2F_{5/2}$} manifold relative intensity at high doping concentrations can also be explained in a similar manner.

In addition, Fig. 3a displays a change of the shape of the blue edge of the 1020 nm emission bands. This observation suggests strong self-absorption of the {Er^{3+}:$^4I_{11/2}$ & Yb^{3+}:$^2F_{5/2}$} manifold starting from low Yb^{3+} doping concentration of 3 mol%. This behaviour is expected of Yb^{3+}-doped materials as it was observed in materials with Yb^{3+} doping concentration as low as 1 mol%.[73]

The increase of the Er^{3+} concentration (Fig. 3b) results in a continuous increase of the relative intensity of the {Er^{3+}:$^4I_{11/2}$ & Yb^{3+}:$^2F_{5/2}$} manifold. However, the increase of the relative intensity at 668 nm is observed only for the highest concentration (15 mol%) of Er^{3+}. This behaviour can be explained by two energy transfer processes (Fig. S2, ESI†): (i) $^4F_{7/2} \rightarrow {}^4I_{11/2}$ which is resonant with the $^4I_{15/2} \rightarrow {}^4I_{11/2}$ transition (Fig. S2, ESI,†

transition ②) and (ii) $^4F_{5/2} \rightarrow {}^4F_{9/2}$ which is resonant with the $^4I_{15/2} \rightarrow {}^4I_{13/2}$ transition (Fig. S2, ESI,† transition ③).[72] The contribution of the first energy transfer process can give rise to the {Er^{3+}:$^4I_{11/2}$ & Yb^{3+}:$^2F_{5/2}$} manifold emission. In turn, the contribution of the second process can be responsible for increase of the relative intensity of the $^4F_{9/2}$ level. It is reasonable that the ground state of Er^{3+} is a weaker energy acceptor than the ground state of Yb^{3+} as quenching is observed at a significantly higher concentration of Er^{3+} (15 mol%) as compared to the Yb^{3+} concentration (10 mol%).

The relative ratio of UC emission peaks has a much weaker dependence on the concentrations of the doping ions (Fig. 3c and d). In contrast to UV excitation, the increase in the Yb^{3+} concentration results in a moderate decrease in the 668 nm relative emission. This is due to the fact that the upper level of Er^{3+} is less involved in the UC process. Thus, we assumed that the energy transfer processes from the upper levels of Er^{3+} are unlikely to occur for all investigated samples at excitation intensities up to 490 W cm^{-2}. The significant increase in the

This journal is © The Royal Society of Chemistry 2021

J. Mater. Chem. C, 2021, **9**, 3493–3503 | **3497**

emission at around 800 nm at high Er^{3+} concentrations (Fig. 3d) can be explained by the increasing population of the $^4I_{9/2}$ level from the $^4I_{13/2}$ state due to the resonance of this transition to the $^4S_{3/2} \rightarrow {}^4I_{9/2}$ transition, as shown in Fig. S3 (ESI†) (transition ①). However, these cross-relaxation processes become significant only if the concentration of Er^{3+} is high (>5 mol%). The proposed pathways for the deactivation of upper Er^{3+} levels were also confirmed *via* measurements of excitation spectra for the Er^{3+}: $^4F_{9/2}$ energy level monitored at 660 nm (Fig. S4, ESI†).

Luminescence decay

The luminescence decay kinetics of the $^2H_{9/2}$, $^4S_{3/2}$, $^4F_{9/2}$, $^4I_{13/2}$ levels of the Er^{3+} ions as well as the $\{Er^{3+}:{}^4I_{11/2}$ & $Yb^{3+}:{}^2F_{5/2}\}$ manifold are recorded using two excitation sources: a 976 nm diode laser (excitation of the $^2F_{5/2}$ level of the Yb^{3+} ions) and a 375 nm LED (excitation of the $^4G_{11/2}$ level of the Er^{3+} ions). The obtained curves are given in Fig. S5–S8 (ESI†). All of the luminescence decay curves except those at 540 nm exhibit mono-exponential behaviour under 375 nm and 976 nm excitations. In the case of $^4S_{3/2} \rightarrow {}^4I_{15/2}$ (540 nm) transition, the decay demonstrates strong non-mono exponential behaviour (see Fig. S6a and b, ESI†) and therefore it was fitted with a double exponential function (eqn (2)) that gives a good level of conformity between the fit and the experimental data.

$$I = A_1 e^{-\frac{t}{\tau_1}} + A_2 e^{-\frac{t}{\tau_2}} \qquad (2)$$

The mean decay times presented in Fig. 4 and Table S2 (ESI†) are calculated using eqn (3)[74]

$$\tau = \frac{A_1\tau_1^2 + A_2\tau_2^2}{A_1\tau_1 + A_2\tau_2} \qquad (3)$$

Fig. 4 indicates that under 375 nm excitation the increase in Yb^{3+} and Er^{3+} concentration leads to a decrease in the decay times of both $^4S_{3/2}$ and $^4F_{9/2}$ energy levels. This decrease can be explained by the excitation energy migration within an excited state manifold. If an excitation migrates until it meets a quenching centre, the migration process reduces the decay time of the excited state.[75] The quenching process can be based on cross-relaxation or interaction with a ground state (for instance the cross-relaxation with the resonance between $^4S_{3/2} \rightarrow {}^4I_{9/2}$ and $^4I_{13/2} \rightarrow {}^4I_{9/2}$ transitions (Fig. S3, ESI,† transition ①)) or interaction of the $^4H_{11/2}$ level with the Er^{3+} ground state: $^4H_{11/2} \rightarrow {}^4I_{13/2}$ is resonant with $^4F_{15/2} \rightarrow {}^4I_{9/2}$ (Fig. S3, ESI,† transition ②). In addition, the observed decay time can also decrease, if the increased Ln^{3+} ion concentration affects the crystal lattice and thereby the lifetimes of radiative transitions. For instance, previously we observed an increase in the absorption cross-section (absorption enhancement) with the increase of the dopant concentration (Table 1). We can assume that the radiative rate also increases with the increase of Yb^{3+} and Er^{3+} concentration that results in an additional drop in the decay time.

Under 976 nm excitation the decay times of the $^4S_{3/2}$ and $^4F_{9/2}$ energy levels are extended compared to the decay times

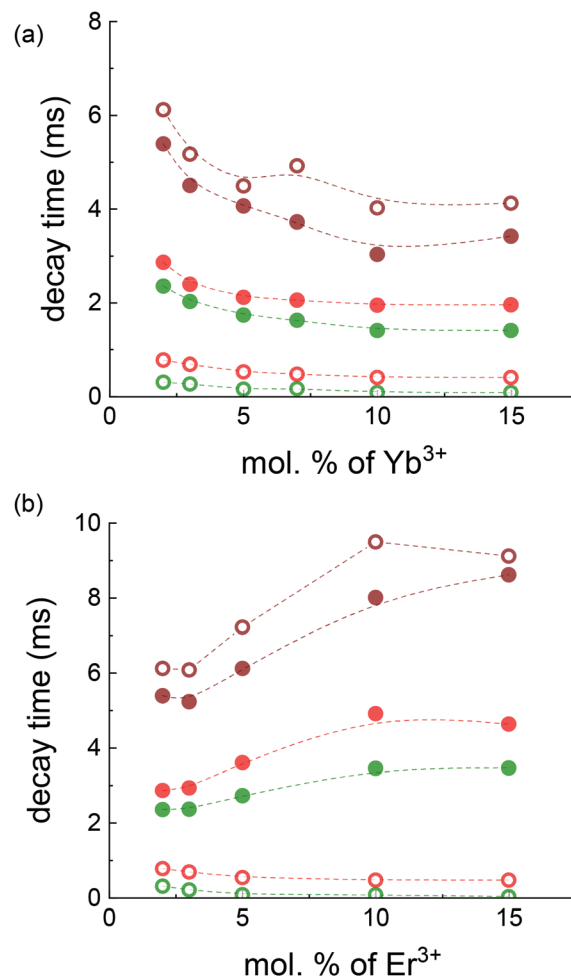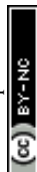**Fig. 4** Luminescence decay time of $^4S_{3/2} \rightarrow {}^4I_{15/2}$ (green symbols) and $^4F_{9/2} \rightarrow {}^4I_{15/2}$ (red symbols) transitions of the Er^{3+} ions as well as decay time of $\{Er^{3+}:{}^4I_{11/2}$ & $Yb^{3+}:{}^2F_{5/2}\}$ manifold (brown symbols) under 375 nm (empty symbols) and 976 nm (filled symbols) excitation as a function of Yb^{3+} (a) and Er^{3+}(b) nominal concentrations. The dashed lines are a guide to the eye. The exact decay times are presented in Table S1 (ESI†).

obtained under 375 nm excitation. This proves that in the case of UC excitation, the population of the higher states of the Er^{3+} ions is governed by energy transfer from long-lived intermediate states with lower energy. For instance, the decay time of the $^4S_{3/2}$ level reflects the long decay time of the $\{Er^{3+}:{}^4I_{11/2}$ & $Yb^{3+}:{}^2F_{5/2}\}$ manifold. At higher Yb^{3+} concentrations the decay time of the $\{Er^{3+}:{}^4I_{11/2}$ & $Yb^{3+}:{}^2F_{5/2}\}$ manifold decreases due to ETU enhancement. This effect leads to the shortening of $^4S_{3/2}$ decay time at a high Yb^{3+} content. In contrast, at higher Er^{3+} concentrations the decay time of the $^4S_{3/2}$ level under 976 nm excitation becomes longer. This again reflects the increase of the $\{Er^{3+}:{}^4I_{11/2}$ & $Yb^{3+}:{}^2F_{5/2}\}$ manifold decay time with the increase of the Er^{3+} concentration.

This trend in the decay time behaviour for the $\{Er^{3+}:{}^4I_{11/2}$ & $Yb^{3+}:{}^2F_{5/2}\}$ manifold – it decreases with the increase in the Yb^{3+} concentration, but increases with the increase in the Er^{3+} content for both excitation types – is quite an interesting observation, as both ions are from the same $\{Er^{3+}:{}^4I_{11/2}$ & $Yb^{3+}:{}^2F_{5/2}\}$ manifold.

3498 | *J. Mater. Chem. C*, 2021, **9**, 3493–3503

This journal is © The Royal Society of Chemistry 2021

Under certain conditions, the prolongation of the decay time can be attributed to the effect of reabsorption, when luminescence is reabsorbed and reemitted several times within the same crystal. However, the reabsorption of 1020 nm emission can have only a minor effect (Fig. 3b) and cannot explain the increase of {Er^{3+}:$^4I_{11/2}$ & Yb^{3+}:$^2F_{5/2}$} manifold decay time with the increase in the Er^{3+} concentration. Alternatively, the increase of {Er^{3+}:$^4I_{11/2}$ & Yb^{3+}:$^2F_{5/2}$} manifold decay time observed under 976 nm excitation can reflect the fact that the lifetime of Er^{3+}:$^4I_{11/2}$ is much longer than the lifetime of the Yb^{3+}:$^2F_{5/2}$ state. For instance, the lifetimes of 7.41 ms and 0.77 ms were measured for single Er^{3+} doped (5 mol%) and single Yb^{3+} doped (5 mol%) BaF_2 crystals, respectively (Fig. S9, ESI†). Thus, an increase in the Er^{3+} concentration should increase the contribution of the long-lived Er^{3+}:$^4I_{11/2}$ state to the decay time of the {Er^{3+}:$^4I_{11/2}$ & Yb^{3+}:$^2F_{5/2}$} manifold, and increase it.

The additional prolongation of the {Er^{3+}:$^4I_{11/2}$ & Yb^{3+}:$^2F_{5/2}$} manifold decay time observed under 375 nm excitation at a high Er^{3+} concentration can be explained by the increasing role of the Er^{3+}:$^4I_{9/2}$ level in the {Er^{3+}:$^4I_{11/2}$ & Yb^{3+}:$^2F_{5/2}$} manifold population. Fig. S3 (ESI†) demonstrates a number of possible ways (① and ②) by which the Er^{3+}:$^4I_{9/2}$ level can be populated by a further transition to the {Er^{3+}:$^4I_{11/2}$ & Yb^{3+}:$^2F_{5/2}$} manifold. In the crystals with low maximum phonon energy (240 cm^{-1} for BaF_2), the rate of multiphonon relaxation for the $^4I_{9/2} \rightarrow {}^4I_{11/2}$ transition (with the energy gap of $\Delta E = 2000$ cm^{-1}) is very slow and, thus, the decay time approaches the radiative lifetime of the $^4I_{9/2}$ state after 10 ms.[76] Thus, this weakly emissive, but long-lived state can be considered as an additional reservoir (in parallel with the {Er^{3+}:$^4I_{11/2}$ & Yb^{3+}:$^2F_{5/2}$} manifold and the Er^{3+}:$^4I_{13/2}$ state) of metastable excited states influencing the DS and UC processes. Under this circumstance, the moderate and high concentrations of Er^{3+} contribute to the population of the $^4I_{9/2}$ state increasing the lifetime of $^4S_{3/2}$, $^4F_{9/2}$, and {Er^{3+}:$^4I_{11/2}$ & Yb^{3+}:$^2F_{5/2}$} states.

Quantum yield

The UC quantum yield ϕ_{UC} is the main figure-of-merit parameter, which can help to understand the physical mechanism and practical value of the UC process. The ϕ_{UC}, as it was introduced previously, is the internal quantum yield. The internal quantum yield characterizes the conversion efficiency of absorbed photons into emitted photons. However, the parameter of brightness (B), which depends also on a number of absorbed photons, is more important for some applications.[77] It can be calculated as:

$$B = \phi_{UC} \times \alpha \quad (4)$$

where α is the absorption coefficient.

The highest ϕ_{UC} and brightness values for the UC emission integrated in the 400–900 nm range as well as the ϕ_{UC} values of certain emission bands are given in Table 2. Additionally, the ϕ_{UC} values of the $^2H_{11/2}$–$^4I_{15/2}$, $^4I_{9/2}$–$^4I_{15/2}$ and $^4S_{3/2}$–$^4I_{13/2}$ are presented in Table S3 (ESI†) and ϕ_{DS} values under 375 nm excitation are noted in Table S4 (ESI†). The highest measured

Table 2 Maximum ϕ_{UC} (at an intensity of 490 W cm^{-2}) for $^4S_{3/2} \rightarrow {}^4I_{15/2}$, and $^4F_{9/2} \rightarrow {}^4I_{15/2}$ transitions of Er^{3+} emission and total ϕ_{UC} in the 400–900 nm range under 976 nm excitation

	$^4S_{3/2} \rightarrow {}^4I_{15/2}$	$^4F_{9/2} \rightarrow {}^4I_{15/2}$	Total	Brightness, cm^{-1}
Er2Yb2	0.021	0.063	0.099	0.121
Er2Yb3	0.023	0.061	0.100	0.192
Er2Yb5	0.021	0.053	0.088	0.262
Er2Yb7	0.023	0.043	0.081	0.374
Er2Yb10	0.019	0.036	0.068	0.495
Er2Yb15	0.013	0.027	0.048	0.419
Er3Yb3	0.018	0.043	0.064	0.120
Er5Yb3	0.017	0.03	0.062	0.148
Er10Yb3	0.008	0.01	0.026	0.121
Er15Yb3	0.002	0.004	0.011	0.065

ϕ_{UC} values reach 9.9% and 10.0% under an excitation intensity of 490 W cm^{-2} in the samples doped with 2% of Er^{3+} as well as 2 and 3% of Yb^{3+} ions, respectively. These results significantly exceed the ϕ_{UC} values of 6.5% observed in the SrF_2 single crystals[23] as well as 2.8% observed in SrF_2 nano- and microparticles[61] doped with Er^{3+} and Yb^{3+} ions.[22,23] At the same time the sample doped with 2% of Er^{3+} and 10% of Yb^{3+} demonstrates the highest brightness value.

This composition should provide the largest number of emitted photons per volume and can be optimal for UC applications of luminescent BaF_2:Yb^{3+}, Er^{3+} materials.

The power dependent ϕ_{UC} under 976 nm excitation is summarized in Fig. 5, where the following trends can be observed: (i) under lower excitation intensity (<100 W cm^{-2}) the samples exhibit an increase of ϕ_{UC} with the increase of the Yb^{3+} concentration; (ii) in contrast, under high excitation intensity, a reduced concentration of Yb^{3+} is preferable for achieving higher ϕ_{UC} values; (iii) increase of Er^{3+} concentration results in increased ϕ_{UC} at intensity <10 W cm^{-2}, and lowered ϕ_{UC} in the broad intensity range (10–490 W cm^{-2}). A similar effect was also observed in β-$NaYF_4$ doped with Er^{3+}.[78]

Another UC figure-of-merit parameter, critical power density (CPD), is calculated for each sample using an earlier published method.[60] This parameter describes the saturation ϕ_{UC} and facilitates the comparison of different UC materials. Combined with the maximum ϕ_{UC} value, it can provide a full set of characteristics required for the analysis of application perspectives of UC materials.

The beneficial low CPD values of the $^4S_{3/2} \rightarrow {}^4I_{15/2}$ transition of the Er^{3+} ions were earlier reported for the most efficient UC materials as 0.7 W cm^{-2} in β-$NaYF_4$, 1.0 W cm^{-2} in YF_3 and 1.0 W cm^{-2} in La_2O_3.[60] The smallest CPD value of the $^4S_{3/2} \rightarrow {}^4I_{15/2}$ transition in the BaF_2 crystal (with 2% of Er^{3+}, 15% of Yb^{3+} ions) is 1.1 W cm^{-2}, which is just fractionally higher than the values calculated for the best UC materials. Table S5 (ESI†) shows the results for the samples that provided the best fit.

Possible heating of samples was considered during the intensity-dependent measurements. To monitor a possible change of the sample temperature an approach from the literature[79] was utilized. The ratio between $^2H_{11/2}$–$^4I_{15/2}$ (521 nm) and $^4S_{3/2}$–$^4I_{15/2}$ (545 nm) emission bands was calculated. The results are presented in Fig. S10 (ESI†). They show that

This journal is © The Royal Society of Chemistry 2021

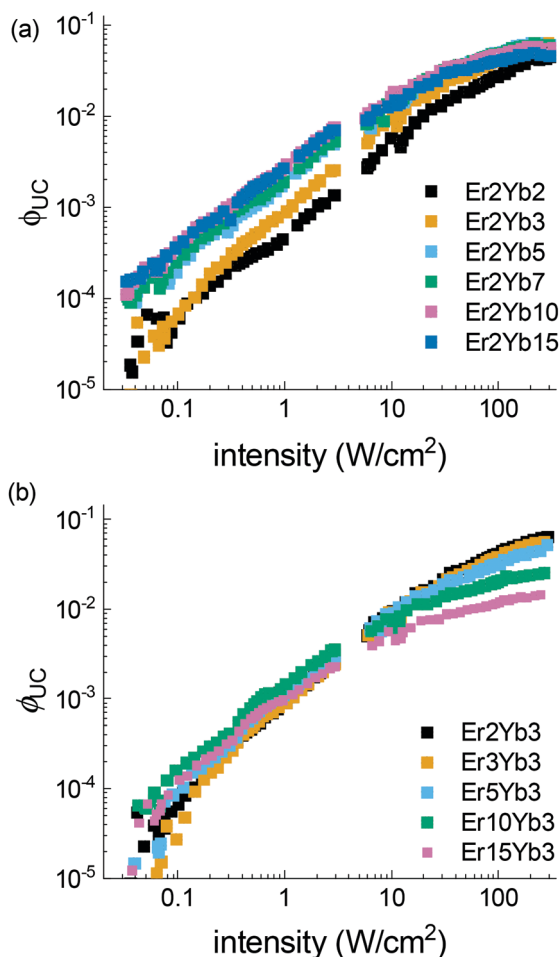*J. Mater. Chem. C*, 2021, **9**, 3493–3503 | **3499**

Fig. 5 Intensity dependence of the UC quantum yield (ϕ_{UC}) under 976 nm excitation.

noticeable heating is observable only at the highest power densities (> 200 W cm^{-2}) in the samples with high Yb^{3+} and Er^{3+} doping concentrations. We assume that the increase of sample temperature can be responsible for the drop of ϕ_{UC} observed at intensity > 200 W cm^{-2} for samples with high doping concentrations.

A more detailed study of the down-shifting emission of the $^4S_{3/2}$ and $^4F_{9/2}$ levels at direct excitation (522 nm for $^4S_{3/2}$ and 652 nm for $^4F_{9/2}$) should help to have a deeper insight into the UC process efficiency. We observed that the ϕ_{DS} of the 540 nm emission under 522 nm excitation is in the range of 1–4% and ϕ_{DS} of the 660 nm emission under 652 nm excitation is in the range of 15–26% (Table S6, ESI†). Additionally, the ϕ_{DS} values of $^4F_{9/2}$–$^4I_{15/2}$, $^4I_{9/2}$–$^4I_{15/2}$ and $^4S_{3/2}$–$^4I_{13/2}$ emission bands under 522 nm excitation can be found in Table S7 (ESI†).

It is clear that the value of ϕ_{DS} gives an indication of the maximum achievable ϕ_{UC} for this particular level. It cannot exceed half of this value ($\phi_{DS} \leq 4\%$ for $^4S_{3/2} \rightarrow ^4I_{15/2}$ transition and $\phi_{DS} \leq 26\%$ in case of $^4F_{9/2} \rightarrow ^4I_{15/2}$ transition) due to the fact that the UC process involves at least two photons. The lack of any strong dependence on the Yb^{3+} concentration in both cases means that there are no transitions from $^4S_{3/2}$ and $^4F_{9/2}$

levels of Er^{3+} interacting with the ground state of Yb^{3+}. However, in both cases, there is a strong drop in ϕ_{DS} values with the increase in the Er^{3+} concentration. This may prove that there is a strong energy migration and quenching within the Er^{3+}:$^4S_{3/2}$ state even at relatively low Er^{3+} concentrations like 5% as it was assumed in the Luminescence Decay section.
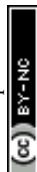
Judd–Ofelt analysis

The experimental lifetimes are compared with radiative lifetimes of some levels of the Er^{3+} ions, which is calculated using the Judd–Ofelt theory by the standard procedure.[80,81] The detailed description of transition probability calculation is presented in the corresponding section of the ESI.†

Knowing the transition probabilities, it is possible to calculate the radiative decay time (τ_r) of a level and the corresponding branching ratio (β). These results together with experimentally measured decay times (τ) upon the direct excitation of the corresponding level in Er^{3+} ions (Fig. S11, ESI†) can help to predict the quantum yield value (ϕ_{DS}^{calc}) for three transitions: $^4S_{3/2} \rightarrow ^4I_{15/2}$, $^4F_{9/2} \rightarrow ^4I_{15/2}$ and $^4I_{13/2} \rightarrow ^4I_{15/2}$. The resulting ϕ_{DS}^{calc} values were calculated using eqn (8) and are summarized in Table S9 (ESI†) together with τ, τ_r, β.

$$\phi_{DS}^{calc} = \frac{\tau}{\tau_r}\beta \tag{8}$$

These results provide an insight into the possible application of the Judd–Ofelt theory to study UC and DS processes in Ln^{3+} co-doped systems. Altogether, the obtained values of the radiative decay times are close to the results of other studies devoted to optical properties of Er^{3+} ions in fluoride single crystals and micropowders.[76,82–84]

Although an acceptable level of conformity between theoretical prediction (ϕ_{DS}^{calc} in Table S9, ESI†) and experimental results (ϕ_{DS} in Table S6, ESI†) for the $^4F_{9/2} \rightarrow ^4I_{15/2}$ transition exists (the relative difference ($\phi_{DS} - \phi_{DS}^{calc})/\phi_{DS}$ doesn't exceed 20% in most cases), in the case of $^4S_{3/2} \rightarrow ^4I_{15/2}$ and $^4I_{13/2} \rightarrow ^4I_{15/2}$ transitions a discrepancy between quantum yields extracted from the Judd–Ofelt calculation and the experimental one is significant. The values of ϕ_{DS}^{calc} estimated via Judd–Ofelt analysis always exceed unity for the $^4I_{13/2} \rightarrow ^4I_{15/2}$ transition, because the measured decay times (τ) are longer than predicted radiative lifetimes (τ_r). Unfortunately, it remains unclear whether Judd–Ofelt theory describes well the $^4I_{13/2} \rightarrow ^4I_{15/2}$ transition with strong magnetic dipole contribution or there is another energy transfer process and/or strong emission reabsorption leading to the elongation of the decay time. For the $^4S_{3/2} \rightarrow ^4I_{15/2}$ transition, the predicted values of ϕ_{DS}^{calc} also overestimate the quantum yield in all investigated samples. We observed again the elongation of the decay times combined with rather small values of ϕ_{DS} measured experimentally. This discrepancy is observed along with the strong deviation of $^4S_{3/2} \rightarrow ^4I_{15/2}$ decays from the single-exponential behaviour (Fig. S11, ESI†) and can indicate the existence of an energy transfer pathway (energy migration[85] thermal coupling between $^4S_{3/2}$ and $^2H_{11/2}$ states,[86] for instance) and/or strong emission

3500 | J. Mater. Chem. C, 2021, **9**, 3493–3503

This journal is © The Royal Society of Chemistry 2021

reabsorption which cannot be described using our simplified model. However, we believe that in our future work including Yb^{3+} and Er^{3+} single-doped crystals with a concentration range starting from very low dopant concentrations (0.1 mol%) we will be able to explain this interesting behaviour.

Conclusions

Optical properties of co-doped BaF_2 single crystals were investigated for a broad range of Er^{3+} (2–15 mol%) and Yb^{3+} (2–15 mol%) doping concentrations. All samples demonstrate efficient UC emission under 976 nm excitation. A very high ϕ_{UC} value of 10.0% (at 490 W cm^{-2}) was observed for the sample doped with 2% of Er^{3+} and 3% of Yb^{3+}. This value exceeds previously reported ϕ_{UC} for SrF_2 single crystals (6.5%) and approaches the efficiency of the best UC material known to date ($NaYF_4$:Yb^{3+}, Er^{3+} with a quantum yield of 11%[21]). The investigation of UC and DS luminescent spectra, lifetimes and quantum yields under multiple excitation wavelengths of 375, 522, 653, 976 and 1520 nm, as well as a comparison of the experimental results with predictions of Judd–Ofelt theory highlights the complexity of the UC process. More specifically, our results demonstrate a significant reduction of luminescence quantum yield of the Er^{3+}:$^4S_{3/2}$ state in the DS regime, which in turn reduces the quantum yield of its emission in UC regimes. Due to the low maximum phonon energy of BaF_2 crystals (240 cm^{-1}), we observed an unusually strong contribution of the Er^{3+}:$^4I_{9/2}$ state in the temporal behaviour of both UC and DS processes.

Author contributions

The manuscript was written through the contribution from all authors. E. M. and D. B. conducted spectroscopy experiments and E. M. wrote the paper. V. A. K. and A. N. N. grew the BaF_2 single crystals. T. B. performed WDXRF analysis of the chemical composition. S. V. K., A. T. and C. W. developed the original concept of the paper. P. P. V., I. A. H. and B. S. R. contributed equally to scoping and structuring the paper and provided additional guidance on experimental methods. All authors have approved the final version of the manuscript.

Conflicts of interest

There are no conflicts to declare.

Acknowledgements

Notes and references

1 S. V. Eliseeva and J.-C. G. Bünzli, *Chem. Soc. Rev.*, 2010, **39**, 189–227.

2 J. Thirumalai, *Luminescence - An Outlook on the Phenomena and their Applications*, InTech, 2016.

3 X. Li, S. Lu, D. Tu, W. Zheng and X. Chen, *Nanoscale*, 2020, **12**, 15021–15035.

4 Y. Liu, D. Tu, H. Zhu and X. Chen, *Chem. Soc. Rev.*, 2013, **42**, 6924–6958.

5 Y. I. Park, J. H. Kim, K. T. Lee, K. S. Jeon, H. B. Na, J. H. Yu, H. M. Kim, N. Lee, S. H. Choi, S. I. Baik, H. Kim, S. P. Park, B. J. Park, Y. W. Kim, S. H. Lee, S. Y. Yoon, I. C. Song, W. K. Moon, Y. D. Suh and T. Hyeon, *Adv. Mater.*, 2009, **21**, 4467–4471.

6 S. Xu, S. Huang, Q. He and L. Wang, *Trends Anal. Chem.*, 2015, **66**, 72–79.

7 D. V. Pominova, A. V. Ryabova, K. G. Linkov, I. D. Romanishkin, S. V. Kuznetsov, J. A. Rozhnova, V. I. Konov and V. B. Loschenov, *Laser Phys.*, 2016, **26**, 084001.

8 Q. Dai, M. E. Foley, C. J. Breshike, A. Lita and G. F. Strouse, *J. Am. Chem. Soc.*, 2011, **133**, 15475–15486.

9 H.-A. Park, Y. K. Lee, W. B. Im, J. Heo and W. J. Chung, *Opt. Mater.*, 2015, **41**, 67–70.

10 R. C. Evans, P. Douglas and C. J. Winscom, *Coord. Chem. Rev.*, 2006, **250**, 2093–2126.

11 J. C. Goldschmidt and S. Fischer, *Adv. Opt. Mater.*, 2015, **3**, 510–535.

12 B. M. van der Ende, L. Aarts and A. Meijerink, *Phys. Chem. Chem. Phys.*, 2009, **11**, 11081–11095.

13 A. S. Nizamutdinov, S. V. Kuznetsov, E. I. Madirov, V. V. Voronov, A. R. Khadiev, A. D. Yapryntsev, V. K. Ivanov, V. V. Semashko and P. P. Fedorov, *Opt. Mater.*, 2020, **108**, 110185.

14 R. G. Geitenbeek, P. T. Prins, W. Albrecht, A. van Blaaderen, B. M. Weckhuysen and A. Meijerink, *J. Phys. Chem. C*, 2017, **121**, 3503–3510.

15 J. Rocha, C. D. S. Brites and L. D. Carlos, *Chem. – Eur. J.*, 2016, **22**, 14782–14795.

16 M. S. Pudovkin, O. A. Morozov, V. V. Pavlov, S. L. Korableva, E. V. Lukinova, Y. N. Osin, V. G. Evtugyn, R. A. Safiullin and V. V. Semashko, *J. Nanomater.*, 2017, **2017**, 3108586.

17 D. Jaque and F. Vetrone, *Nanoscale*, 2012, **4**, 4301–4326.

18 J. Andres, R. D. Hersch, J.-E. Moser and A.-S. Chauvin, *Adv. Funct. Mater.*, 2014, **24**, 5029–5036.

19 P. Kumar, S. Singh and B. K. Gupta, *Nanoscale*, 2016, **8**, 14297–14340.

20 I. Etchart, A. Huignard, M. Bérard, M. N. Nordin, I. Hernández, R. J. Curry, W. P. Gillin and A. K. Cheetham, *J. Mater. Chem.*, 2010, **20**, 3989–3994.

This journal is © The Royal Society of Chemistry 2021

J. Mater. Chem. C, 2021, **9**, 3493–3503 | **3501**

21 M. Kaiser, C. Würth, M. Kraft, I. Hyppänen, T. Soukka and U. Resch-Genger, *Nanoscale*, 2017, **9**, 10051–10058.

22 M. Pokhrel, G. A. Kumar and D. K. Sardar, *J. Mater. Chem. A*, 2013, **1**, 11595–11606.

23 D. Saleta Reig, B. Grauel, V. A. Konyushkin, A. N. Nakladov, P. P. Fedorov, D. Busko, I. A. Howard, B. S. Richards, U. Resch-Genger, S. V. Kuznetsov, A. Turshatov and C. Würth, *J. Mater. Chem. C*, 2020, **8**, 4093–4101.

24 M.-L. Zheng, K. Fujita, W.-Q. Chen, X.-M. Duan and S. Kawata, *J. Phys. Chem. C*, 2011, **115**, 8988–8993.

25 Y. Zhong, I. Rostami, Z. Wang, H. Dai and Z. Hu, *Adv. Mater.*, 2015, **27**, 6418–6422.

26 A. Ishii, Y. Adachi, A. Hasegawa, M. Komaba, S. Ogata and M. Hasegawa, *Sci. Technol. Adv. Mater.*, 2019, **20**, 44–50.

27 F. Auzel, *Chem. Rev.*, 2004, **104**, 139–173.

28 V. V. Ovsyankin and P. P. Feofilov, *J. Exp. Theor. Phys.*, 1966, **3**, 322.

29 D. C. Rodriguez Burbano, R. Naccache and J. A. Capobianco, *Handbook on the Physics and Chemistry of Rare Earths*, Elsevier, 2015, vol. **47**, pp. 273–347.

30 X. Zhang, X. Liu, J. P. Jouart and G. Mary, *Chem. Phys. Lett.*, 1998, **287**, 659–662.

31 F. Vetrone, J. C. Boyer, J. A. Capobianco, A. Speghini and M. Bettinelli, *J. Phys. Chem. B*, 2002, **106**, 5622–5628.

32 J. F. Suyver, J. Grimm, K. W. Krämer and H. U. Güdel, *J. Lumin.*, 2005, **114**, 53–59.

33 H. Guo and Y. M. Qiao, *Opt. Mater.*, 2009, **31**, 583–589.

34 X. P. Chen, W. J. Zhang and Q. Y. Zhang, *Phys. B*, 2011, **406**, 1248–1252.

35 A. Pandey, V. K. Rai, R. Dey and K. Kumar, *Mater. Chem. Phys.*, 2013, **139**, 483–488.

36 F. Vetrone, V. Mahalingam and J. A. Capobianco, *Chem. Mater.*, 2009, **21**, 1847–1851.

37 F. C. Guinhos, P. C. Nóbrega and P. A. Santa-Cruz, *J. Alloys Compd.*, 2001, **323**, 358–361.

38 G. Buse, E. Preda, M. Stef, A. Pruna, F. Stef and I. Nicoara.

39 Y. Tian, R. Xu, L. Hu and J. Zhang, *Opt. Mater.*, 2011, **34**, 308–312.

40 H. Wu, Z. Hao, L. Zhang, X. Zhang, Y. Xiao, G.-H. Pan, H. Wu, Y. Luo, H. Zhao and J. Zhang, *J. Phys. Chem. C*, 2018, **122**, 9611–9618.

41 M. J. Weber, *Phys. Rev.*, 1967, **157**, 262–272.

42 D. G. Mead and G. R. Wilkinson, *J. Phys. C: Solid State Phys.*, 1977, **10**, 1063–1072.

43 S. Balabhadra, M. F. Reid, V. Golovko and J.-P. R. Wells, *J. Alloys Compd.*, 2020, **834**, 155165.

44 R. Reisfeld and C. K. Jørgensen, in *Lasers and Excited States of Rare Earths*, ed. R. Reisfeld and C. K. Jørgensen, Springer Berlin Heidelberg, Berlin, Heidelberg, 1977, , DOI: 10.1007/978-3-642-66696-4_1, pp. 1–63.

45 C. Labbe, J. L. Doualan, P. Camy, R. Moncorgé and M. Thuau, *Opt. Commun.*, 2002, **209**, 193–199.

46 A. M. Golubev, L. P. Otroshchenko, V. N. Molchanov, L. E. Fykin and B. P. Sobolev, *Crystallogr. Rep.*, 2009, **54**, 423–430.

47 A. Maaoui, M. Haouari, A. Bulou, B. Boulard and H. Ben Ouada, *J. Lumin.*, 2018, **196**, 1–10.

48 L. N. Ignatieva, N. V. Surovtsev, E. B. Merkulov, N. N. Savchenko, S. V. Adichtchev, Y. V. Marchenko and V. M. Bouznik, *J. Non-Cryst. Solids*, 2012, **358**, 3248–3254.

49 K. Linganna, R. Narro-García, P. Manasa, H. Desirena, E. De la Rosa and C. K. Jayasankar, *J. Rare Earths*, 2018, **36**, 58–63.

50 X. Qiao, X. Fan, M. Wang and X. Zhang, *J. Non-Cryst. Solids*, 2008, **354**, 3273–3277.

51 S. Fischer, N. D. Bronstein, J. K. Swabeck, E. M. Chan and A. P. Alivisatos, *Nano Lett.*, 2016, **16**, 7241–7247.

52 C. Würth, M. Kaiser, S. Wilhelm, B. Grauel, T. Hirsch and U. Resch-Genger, *Nanoscale*, 2017, **9**, 4283–4294.

53 M. Kraft, C. Würth, V. Muhr, T. Hirsch and U. Resch-Genger, *Nano Res.*, 2018, **11**, 6360–6374.

54 R. Arppe, I. Hyppänen, N. Perälä, R. Peltomaa, M. Kaiser, C. Würth, S. Christ, U. Resch-Genger, M. Schäferling and T. Soukka, *Nanoscale*, 2015, **7**, 11746–11757.

55 P. A. Popov, P. P. Fedorov, S. V. Kuznetsov, V. A. Konyushkin, V. V. Osiko and T. T. Basiev, *Dokl. Phys.*, 2008, **53**, 353–355.

56 B. P. Sobolev and N. L. Tkachenko, *J. Less-Common Met.*, 1982, **85**, 155–170.

57 S. V. Kuznetsov and P. P. Fedorov, *Inorg. Mater.*, 2008, **44**, 1434–1458.

58 S. Wen, J. Zhou, K. Zheng, A. Bednarkiewicz, X. Liu and D. Jin, *Nat. Commun.*, 2018, **9**, 2415.

59 S. Dottermusch, D. Busko, M. Langenhorst, U. W. Paetzold and B. S. Richards, *Opt. Lett.*, 2019, **44**, 29–32.

60 R. E. Joseph, C. Jiménez, D. Hudry, G. Gao, D. Busko, D. Biner, A. Turshatov, K. Krämer, B. S. Richards and I. A. Howard, *J. Phys. Chem. A*, 2019, **123**, 6799–6811.

61 S. Kuznetsov, Y. Ermakova, V. Voronov, P. Fedorov, D. Busko, I. A. Howard, B. S. Richards and A. Turshatov, *J. Mater. Chem. C*, 2018, **6**, 598–604.

62 A. A. Kaminskii, H. Rhee, H. J. Eichler, L. Bohatý, P. Becker and K. Takaichi, *Laser Phys. Lett.*, 2008, **5**, 304–310.

63 R. Shannon, *Acta Crystallogr., Sect. A: Cryst. Phys., Diffr., Theor. Gen. Crystallogr.*, 1976, **32**, 751–767.

64 A. Anderson and F. F. Cleveland, *Phys. Today*, 1974, **27**, 54–55.

65 W. Ma, L. Su, X. Xu, J. Wang, D. Jiang, L. Zheng, X. Fan, C. Li, J. Liu and J. Xu, *Opt. Mater. Express*, 2016, **6**, 409.

66 J. Xu, L. Su, H. Li, D. Zhang, L. Wen, H. Lin and G. Zhao, *Opt. Mater.*, 2007, **29**, 932–935.

67 J. L. Doualan, P. Camy, A. Benayad, M. Von Edlinger, V. Ménard and R. Moncorgé.

68 S. Banerjee, J. Koerner, M. Siebold, Q. Yang, K. Ertel, P. D. Mason, P. J. Phillips, M. Loeser, H. Zhang, S. Lu, J. Hein, U. Schramm, M. C. Kaluza and J. L. Collier, *Opt. Express*, 2013, **21**, A726–A734.

69 M. Velázquez, P. Veber, G. Buşe, Y. Petit, P. Goldner, V. Jubera, D. Rytz, A. Jaffres, M. Peltz, V. Wesemann, P. Aschehough and G. Aka, *Opt. Mater.*, 2015, **39**, 258–264.

70 J. Liu, X. Mateos, H. Zhang, J. Wang, M. Jiang, U. Griebner and V. Petrov, *Opt. Lett.*, 2006, **31**, 2580–2582.

71 F. Auzel, K. E. Lipinska-Kalita and P. Santa-Cruz, *Opt. Mater.*, 1996, **5**, 75–78.

3502 | *J. Mater. Chem. C*, 2021, **9**, 3493–3503

This journal is © The Royal Society of Chemistry 2021

72 A. Baride, P. S. May and M. T. Berry, *J. Phys. Chem. C*, 2020, **124**, 2193–2201.

73 A. Boccolini, J. Marques-Hueso, D. Chen, Y. Wang and B. S. Richards, *Sol. Energy Mater. Sol. Cells*, 2014, **122**, 8–14.

74 J. R. Lakowicz, *Principles of fluorescence spectroscopy*, Springer, 2006.

75 J. Liu, T. Fu and C. Shi, *J. Phys. Chem. C*, 2019, **123**, 9506–9515.

76 A. Bitam, S. Khiari, M. Diaf, H. Boubekri, E. Boulma, C. Bensalem, L. Guerbous and J. P. Jouart, *Opt. Mater.*, 2018, **82**, 104–109.

77 K.-L. Wong, J.-C. G. Bünzli and P. A. Tanner, *J. Lumin.*, 2020, **224**, 117256.

78 S. K. W. MacDougall, A. Ivaturi, J. Marques-Hueso, K. W. Krämer and B. S. Richards, *Sol. Energy Mater. Sol. Cells*, 2014, **128**, 18–26.

79 R. E. Joseph, D. Busko, D. Hudry, G. Gao, D. Biner, K. Krämer, A. Turshatov, B. S. Richards and I. A. Howard, *Opt. Mater.*, 2018, **82**, 65–70.

80 M. P. Hehlen, M. G. Brik and K. W. Krämer, *J. Lumin.*, 2013, **136**, 221–239.

81 A. Lira C, I. Camarillo, E. Camarillo, F. Ramos, M. Flores and U. Caldiño, *J. Phys.: Condens. Matter*, 2004, **16**, 5925–5936.

82 E. Preda, M. Stef, G. Buse, A. Pruna and I. Nicoara, *Phys. Scr.*, 2009, **79**, 035304.

83 Y. Zhang, B. Chen, S. Xu, X. Li, J. Zhang, J. Sun, X. Zhang, H. Xia and R. Hua, *Phys. Chem. Chem. Phys.*, 2018, **20**, 15876–15883.

84 M. Luo, B. Chen, X. Li, J. Zhang, S. Xu, X. Zhang, Y. Cao, J. Sun, Y. Zhang, X. Wang, Y. Zhang, D. Gao and L. Wang, *Phys. Chem. Chem. Phys.*, 2020, **22**, 25177–25183.

85 F. T. Rabouw, P. T. Prins, P. Villanueva-Delgado, M. Castelijns, R. G. Geitenbeek and A. Meijerink, *ACS Nano*, 2018, **12**, 4812–4823.

86 Y. Zhang, B. Chen, S. Xu, X. Li, J. Zhang, J. Sun, X. Zhang, H. Xia and R. Hua, *Phys. Chem. Chem. Phys.*, 2019, **21**, 10840–10845.

This journal is © The Royal Society of Chemistry 2021

J. Mater. Chem. C, 2021, **9**, 3493–3503 | **3503**